Flower-like NiCo 2 O 4 -CN as Efficient bifunctional Electrocatalyst for Zn-Air Battery

Yao Li, Zihao Zhou, Gao Cheng, Shengbo Han, Junli Zhou, Jinkai Yuan, Ming Sun 1 , Lin Yu

Flower-like $NiCo_2O_4$-CN as Efficient bifunctional Electrocatalyst for Zn-Air Battery

Yao Li[1] , Zihao Zhou[1], Gao Cheng[1] , Shengbo Han[1], Junli Zhou[1], Jinkai Yuan[2], Ming Sun[1*] , Lin Yu[1*]

[1]Key Laboratory of Clean Chemistry Technology of Guangdong Regular Higher Education Institutions, Guangzhou Key Laboratory of Clean Transportation Energy Chemistry, School of Chemical Engineering and Light Industry, Guangdong University of Technology, 510006 Guangzhou, P. R.China

[2] Centre de Recherche Paul Pascal, CNRS, Université de Bordeaux, Pessac 33600, France

Abstract:

Bifunctional transition metal oxide based electrocatalysts play an important role in oxygen reduction reaction (ORR) and oxygen evolution reaction (OER) for rechargeable metal-air batteries. Herein, we synthesize a kind of three-dimensional (3D) flower-like composite catalyst with $NiCo_2O_4$ and N doped carbon (NC) derived from g-C_3N_4, under hydrothermal conditions. The best $NiCo_2O_4$-CN catalyst shows a hierarchical structure composed of interconnected nanosheets, and exhibits versatile bifunctional ORR/OER electroactivities with a half-wave potential of 0.81 V for ORR and an overpotential of 383 mV for OER under a current density of 10 mA cm^{-2}. The zinc-air battery with the $NiCo_2O_4$-CN cathode demonstrates superior peak power density (149.6mW cm^{-2}), excellent capacity performance up to 738.7 mAh g^{-1} and considerable durability, showing the feasibility of $NiCo_2O_4$-CN in electrochemical energy devices.

Keywords: $NiCo_2O_4$; oxygen reduction reaction; oxygen evolution reaction; Zn-air battery;

1. Introduction

In view of the global energy security and environmental crisis, renewable energy storage and conversion systems such as supercapacitors, fuel cells, lithium-ion batteries, and metal-air batteries have stimulated much attention and seen great

*Corresponding author at: Email : sunmgz@gdut.edu.cn (Ming SUN); gych@gdut.edu.cn (Lin YU);

achievements. Among these reported clean and sustainable energy devices, rechargeable metal-air batteries are considered to be the most viable energy system owing to their particular characteristics such as low cost, wide availability, high safety and high energy density, which outperform the widely used lithium-ion batteries[1, 2].

One of the key issues that hinder the development of metal-air batteries is the sluggish kinetics process of oxygen reduction reaction (ORR) and oxygen evolution reaction (OER), which requires the assistance of high efficient and stable catalysts. Unfortunately, the requirement of ORR and OER, which happens over the same electrode during the discharge and charge processes, respectively, for the catalyst is different. And this fact increases the complexities: either combine two kinds of catalysts for individual ORR and OER or using bifunctional catalyst. Up to now, much of the study focus on either ORR catalyst or OER catalyst, for example, Pt related materials is the best ORR catalyst, however, it is not suitable for OER. Therefore, if two individual catalysts were used for the working electrode, such concerns as the cost, the manufacturing complexities, and the match/cooperation would arise[1].

To solve such a problem, the design and synthesis of bifunctional ORR/OER catalysts have fueled much interest. Up to now, the reported bifunctional catalysts include non-noble metal catalysts (metal oxides, hydroxides, sulfides, nitrides), carbon-based catalysts (carbon nanotubes, graphene, biomass-derived carbon, heteroatom-doped carbon, or metal-organic frameworks-derived carbon), and their hybrids[2, 3]. Among these catalysts, metal oxides are promising candidates because of the relatively low cost and reasonably high electrochemical activity. The reported metal oxides include manganese oxides, spinel-type metal oxides, perovskite-type metal oxides, *etc*[1, 4].

Among the bifunctional metal oxides, the spinel-type $NiCo_2O_4$, in particular, has attracted much interest due to its fairly low over-potential and corrosion resistivity[5, 6]. Several effective methods have been adopted to modify the electrochemical

activity of $NiCo_2O_4$, and they are briefly classified as following: (1) Morphology engineering. The ORR/OER is an interfacial process, morphology engineering has a great influence on the activity. Through morphology controlling, $NiCo_2O_4$ with larger surface area, porous and 3D hierarchical structure could be fabricated, which could provide more accessible active sites for ORR/OER. Some successful examples are nanowire[7], nano platelet[8], nanosphere[9, 10], and 3D nanoshees[11, 12]; (2) Metal doping. The electronic structure of spinel oxides is highly related to its composition, and the composition adjustment by a third metal doping is an effective strategy to improve the activity. Because of the complementarities and synergic effects between doping metal and Ni-Co, Zn and Fe doping $NiCo_2O_4$ have reported exhibiting superior ORR/OER activity[13, 14]; (3) Introducing oxygen vacancy or creating defect. Surface defects can tune the surface electronic states, and play pivotal roles in electrochemical reaction[15]. The oxygen vacancy can increase electron density and electrical conductivity, and also be the active sites for ORR/OER [9, 16]. Therefore, precisely tailoring oxygen vacancy is regarded as an effective tactic to enhance the ORR/OER performance of $NiCo_2O_4$[11, 17]; (4) Hybrid with carbon. Although considerable achievements have been made on $NiCo_2O_4$, the relatively low conductivity still hamper its potential application. The composites composed by $NiCo_2O_4$ and various kind of carbon material can not only solve the problem of poor conductivity, but also create a synergetic effect, which can dramatically enhance the electrocatalytic activity and durability[18]. For example, graphene [8, 19], carbon nanotube[20], and hollow carbon[21, 22] have been used for the composite $NiCo_2O_4$ electro-catalysts.

Enlightened by the above achievements, herein, we fabricate 3D flower-like composite catalyst with $NiCo_2O_4$ nanosheet and N doped carbon (NC) derived from g-C_3N_4. The design is based on the following consideration: (1) the 3D structure favors for the mass transport (oxygen and ions); (2) two-dimensional nanosheet possesses more surface unsaturated atoms, which is beneficial for catalytic reaction[23]; (3) N doped carbon. On one hand, the introduction of carbon could

increase the conductivity of $NiCo_2O_4$. On the other hand, the NC itself shows certain ORR/OER activity. (4) g-C_3N_4 derived carbon. g-C_3N_4 is known for its high concentration of N, and has been used as the source of N and C to form NC [24, 25] or transition metal-containing nitrogen-doped carbon[26] under high-temperature calcination, which exhibit superior electrochemical activities. In contrast to the high-temperature pyrolysis, we adopt a relatively mild method to convert g-C_3N_4 to NC under hydrothermal condition, and the concentration of N could be tuned by temperature. The formation of NC and $NiCo_2O_4$ is in the same process, resulting in a uniform composite catalyst. Such a hybrid catalyst display excellent ORR/OER performance. For solvothermal or hydrothermal reaction, the reaction temperature, has great effect in the morphology, crystal structure and corresponding activities of the materials. Herein, we choose one extreme low temperature (90 ^{o}C for methanol), and one very high temperature (180 ^{o}C, a relatively safe and high temperature when using oven in our lab) for the synthesis of $NiCo_2O_4$ and NC composites. Because of such big temperature difference and reaction pressure, it could lead to great difference in the catalyst and its catalytic activity.

2. Experimental

2.1 Synthesis of $NiCo_2O_4$ catalyst

g-C_3N_4 was prepared using melamine as chemical source through decomposition at 550 ^{o}C for 3 h under N_2 atmosphere followed by oxidation in air under 500 ^{o}C for 2 h. 0.5 mmol of $Co(NO_3)_2{\cdot}6H_2O$, 0.25 mmol of $Ni(NO_3)_2{\cdot}6H_2O$, and 1.5 mmol of hexamethylenetetramine were dissolved into 12 ml of CH_3OH together with 10 mg of *g*-C_3N_4 under continuous stirring. Then, the solution was sealed into an autoclave and heated to 180 °C for 12 h. After the solvothermal reaction, the precursor was washed with deionized water and ethanol thoroughly, then dried and calcinated under air atmosphere, at 350 °C for 2 h. The obtained sample was denoted as $NiCo_2O_4$-CN-180. Another sample was prepared by the same process, except that the solvothermal temperature was changed to 90 °C, and was denoted as $NiCo_2O_4$-CN-90.

2.2 Characterization

X-ray diffraction (XRD) was recorded by an X-ray diffractometer (PANalytical, MiniFlex 600, Cu Kα). The Brunauer–Emmett–Teller (BET) surface area and Barrett–Joyner–Halenda (BJH) pore size distribution were analyzed on a Micromeritics instrument (ASAP2020). Use X-ray photoelectron spectroscopy (XPS, Escalab 250X, Thermo Fisher) to test the surface chemical properties (Al Ka as X-ray source). The morphology and elemental distribution of the samples were analyzed by transmission electronic microscopy (TEM，Tecnai G20) and field-emission scanning electron microscope (FE-SEM, Hitachi SU8010) equipped with energy-dispersive X-ray spectrometer (EDS). The Fourier transform infrared (FT-IR) spectra were recorded on a Nicolet 6700 spectrometer.

2.3 Electrochemical Measurements

Cyclic voltammetry (CV) and linear sweep voltammograms (LSVs) were tested on an electrochemical workstation (ZAHNER ZENNIUM/IM6) with three-electrode setup : a rotating ring/disk electrode with glass carbon (GC) disk (5 mm diameter), Ag/AgCl (3.5 M KCl), and Pt sheets as the working electrode, the reference electrode, and the counter electrode, respectively. The catalyst ink was composed by mixing 950 μL of isopropanol, 50 μL of 5 *wt*% Nafion and 5 mg of catalyst. The catalyst loading on the GC electrode was 0.318 mg cm^{-2}. The conditions for ORR measurement were: O_2/N_2 saturated 0.1 M KOH as electrolyte; a sweep rate of 50 mV s^{-1} from -0.70 to 0.20 V (*vs* RHE) for CV and a sweep rate of 5 mV s^{-1} from -0.70 to 0.20 V (vs RHE) under different rotation speeds for LSV. The stability was tested by chronopotentiometric curves at 10 mA cm^{-2} for 12 h. The electron transfer number (*n*) and the H_2O_2 conversion ($y_{peroxide}$) was tested by rotating ring-disk electrode (RRDE). Tafel plot was obtained from the LSV curves. OER activity with *iR* correction was tested by scanning at 5 mV s^{-1} from 0.20 to 0.80 V (vs. SCE) with a 1600 rpm rotation speed for the RDE in 1 M KOH. The electrochemical surface area (ECSA) was tested by CV curves at the potential range from 1.10 to 1.20 V vs. RHE. The conductivity of the catalyst was

measured in a two-electrode system on the same electrochemical workstation above-mentioned. The catalyst was separately pressed into pieces, then two electrodes were clamped on both ends. By applying a linear voltage from -0.5 to 0.5 V with the scan rate of 50 mV/s, the change of current density with voltage was recorded. Rechargeable Zn-Air Battery was fabricated with a homemade cell using zinc plate as anode，catalyst sprayed as air-cathode, 0.2 M $Zn(CH_3COO)_2$ and 6 M KOH as the electrolyte. The catalyst slurry is the same as ORR test, the prepared slurry was first doped uniformly on current carrier, then dried under infrared light with a mass loading of about 2.1 mg cm^{-2}. The discharge polarization curves are collected at scanning rate of 5mV s^{-1} .

3. Results and discussion

3.1 Structure and morphology

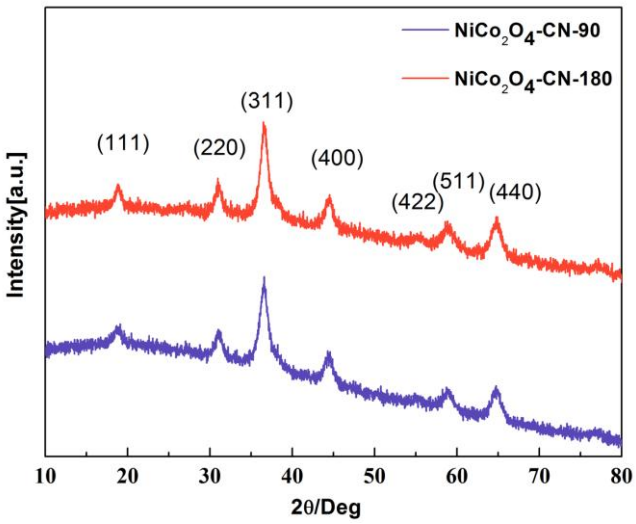

Fig.1 XRD patterns of the $NiCo_2O_4$ samples

The phase structure of the samples was first tested by XRD(Fig.1). For comparison, the pure *g*-C_3N_4 and $NiCo_2O_4$ were also tested and shown in Fig.S1(Supporting information). From Fig.S1, C_3N_4 displays one sharp peak at 2θ =27.2° and two small peaks at 13.1 ° and 21.6 °, which can ascribe to the (001),(100) and (002) crystal plane of *g*-C_3N_4 (JCPDS: 87-1526). The pure $NiCo_2O_4$ shows diffraction peaks correspond to the (111), (220), (311), (400), (422), (511), and (440) planes for the

standard inverse spinel structure of $NiCo_2O_4$ (JCPDS:20-0781). For the two $NiCo_2O_4$ samples synthesized at 90 °C and 180 °C, they exhibit similar XRD patterns as that of the pure $NiCo_2O_4$, and no signal of *g*-C_3N_4 peak is found. This phenomenon could be explained from two aspects: one is that the large amount of $NiCo_2O_4$ in the composite suppresses the *g*-C_3N_4 peak as its content is relatively small compared to the formed $NiCo_2O_4$[27], the other reason is that *g*-C_3N_4 might decompose into carbon.

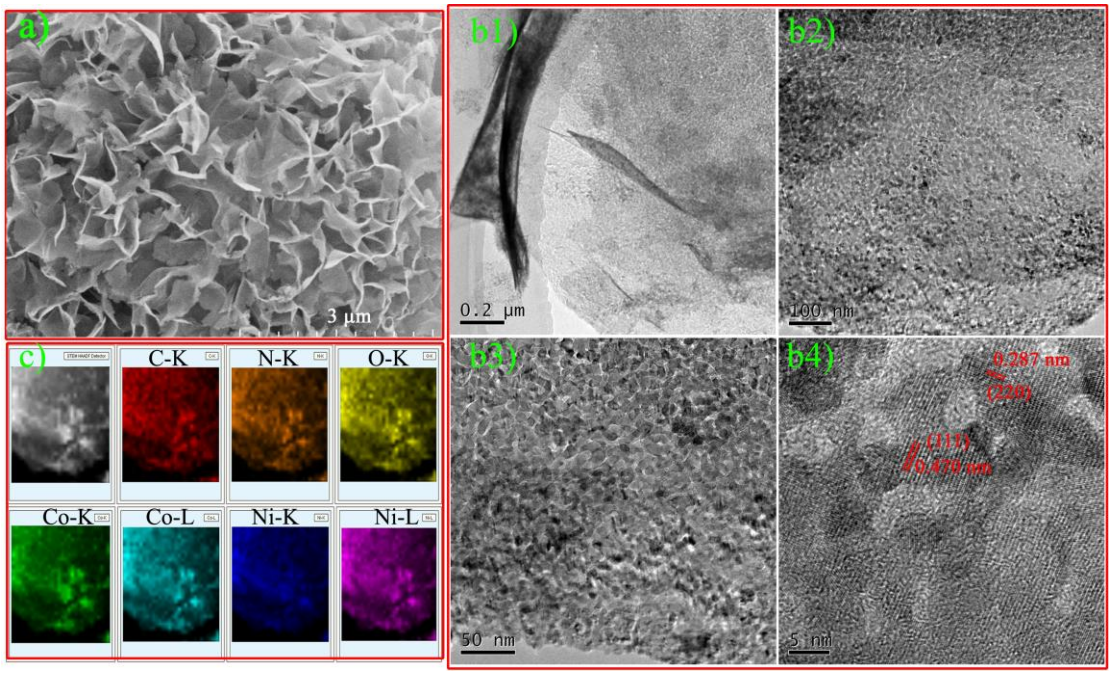

Fig.2 SEM and HRTEM images of the $NiCo_2O_4$-CN sample.

The microstructure of catalyst was observed by SEM and HRTEM techniques as shown in Fig.2 for $NiCo_2O_4$-CN-180 and Fig.S2 for $NiCo_2O_4$-CN-90(Supporting information). From Fig.2, we can detect that $NiCo_2O_4$-CN-180 exhibit 3D flower-like morphology composed by interconnected nanosheets. To show the growth mechanism for the formation of $NiCo_2O_4$-CN, the time-dependent experiment was performed and the corresponding SEM images are supplied in Fig.S3. From Fig. S3, in a very short reaction time, 3D $NiCo_2O_4$ was formed with very large nanosheet. With time prolong, the 3D structure maintains but the nanosheet becomes smaller and integrated with each other to form rich macro-pores. From 6 h until 12 h then to 18 h,

it seems that there is almost no change in the morphology. Based on the fact, we tentatively conclude that the growth of $NiCo_2O_4$ follows the Ostwald Ripening theory. More information about the nanosheet is provided under HRTEM (Fig.2b). The nanosheet is not intact, but with porous nanopores. Two lattice fringes with the interplanar gap of 0.287 nm and 0.470 nm corresponding to the (220) and (111) planes of $NiCo_2O_4$, respectively, are found, which match well with the XRD result. The TEM-mapping result in Fig.2c illustrates the presence and homogeneous distribution of Co, Ni, O from $NiCo_2O_4$, and C, N from *g*-C_3N_4. As for $NiCo_2O_4$-CN-90 (Fig.S2, Supporting information), it shows similar flower-like morphology but with larger size of pore. The lattice spacing of 0.287 nm corresponds to the (220) crystal plane can be observed. The macro- and micro- porous characteristics of the $NiCo_2O_4$ samples could offer more active sites for electrochemical reaction and facilitate the mass and electronic transportation. The SEM-mapping results of the pure *g*-C_3N_4 and $NiCo_2O_4$ composites are supplied in Fig.S4 and the bulk atomic ratio is listed in Table S1(Supporting information). From Fig.S4, all the elements mentioned distribute uniformly over the observation field. As for the bulk atomic ratio of Ni to Co, the two $NiCo_2O_4$ composites have similar value near 0.5. However, great changes could be found for the atomic ratio of C to N, it is 0.63 for *g*-C_3N_4, but increases sharply to 4.95 for $NiCo_2O_4$-CN-90 and 29.02 for $NiCo_2O_4$-CN-180, indicating that *g*-C_3N_4 decomposes into N-doped carbon during the hydrothermal process. The surface molar ratio of C to N by XPS also follows a similar trend(Table S1), further confirming the conclusion.

FT-IR spectra was conducted to show more evidence of the conversion of *g*-C_3N_4 (Fig.S5). For pure *g*-C_3N_4, the peaks between 3000-3400 cm^{-1} correspond to N-H stretching vibration. The peaks in the range of 1200-1700 cm^{-1} can be attributed to the C=N stretching and C-N bonds. The peak locating at 811 cm^{-1} is origin from the out-of-plane bending of heptazine rings[24, 28]. As for pure $NiCo_2O_4$, it mainly displays the peak below 700 cm^{-1}, which is the typical IR spectra of metal oxide. Considering the two $NiCo_2O_4$-CN samples, the characteristic FT-IR peaks between

3000-3400 cm^{-1} disappear, the peaks in the range of 1200-1700 cm^{-1} diminish a lot, the peak at 811 cm^{-1} reduce greatly, and this phenomenon suggest that the C_3N_4 structure in these two samples are destroyed. The two new peaks at 1240 and 1385 cm^{-1} could be assigned to C-O and C-N vibration, respectively. we can also detect the metal–oxide peaks at 650 and 550 cm^{-1}. The FT-IR result prove that *g*-C_3N_4 converts into N doped carbon for the $NiCo_2O_4$-CN sample, which is consistent with the SEM-mapping results.

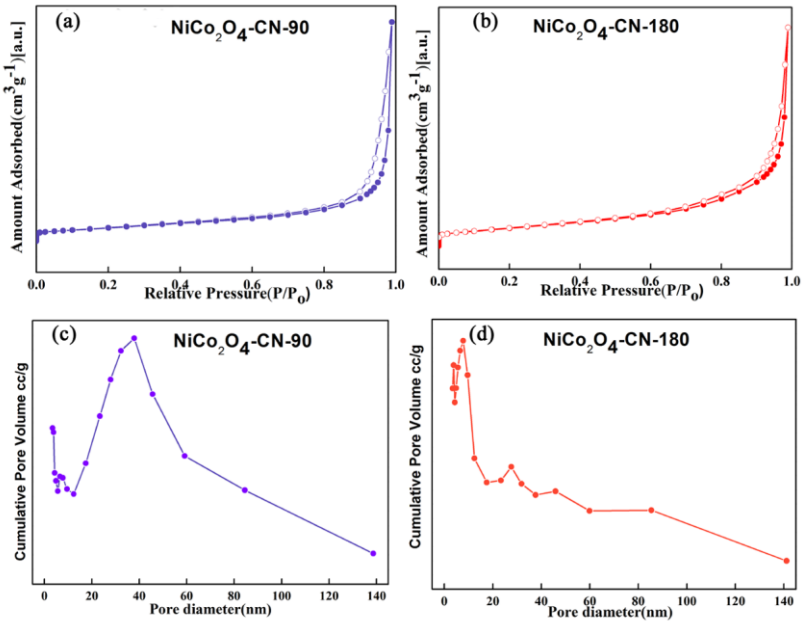

Fig.3 N_2-adsorption/desorption isotherms and BJH pore size distribution of $NiCo_2O_4$ samples

The isotherms and BJH pore size distribution of both samples are shown in Fig.3. They both display type Ⅳ with a distinct hysteresis loop, indicating their mesoporous structures. From the BJH curves, they are both rich in continuous pore and have wide pore size distribution. The measured BET surface area is 84.22 $m^2\ g^{-1}$ for $NiCo_2O_4$-CN-180 and 78.10 $m^2\ g^{-1}$ for $NiCo_2O_4$-CN-90. However, the BJH average pore size of the former is 7.785 nm, which is smaller than that of the latter (37.835 nm). This phenomenon confirms that $NiCo_2O_4$-CN-180 is richer in narrow size of pore.

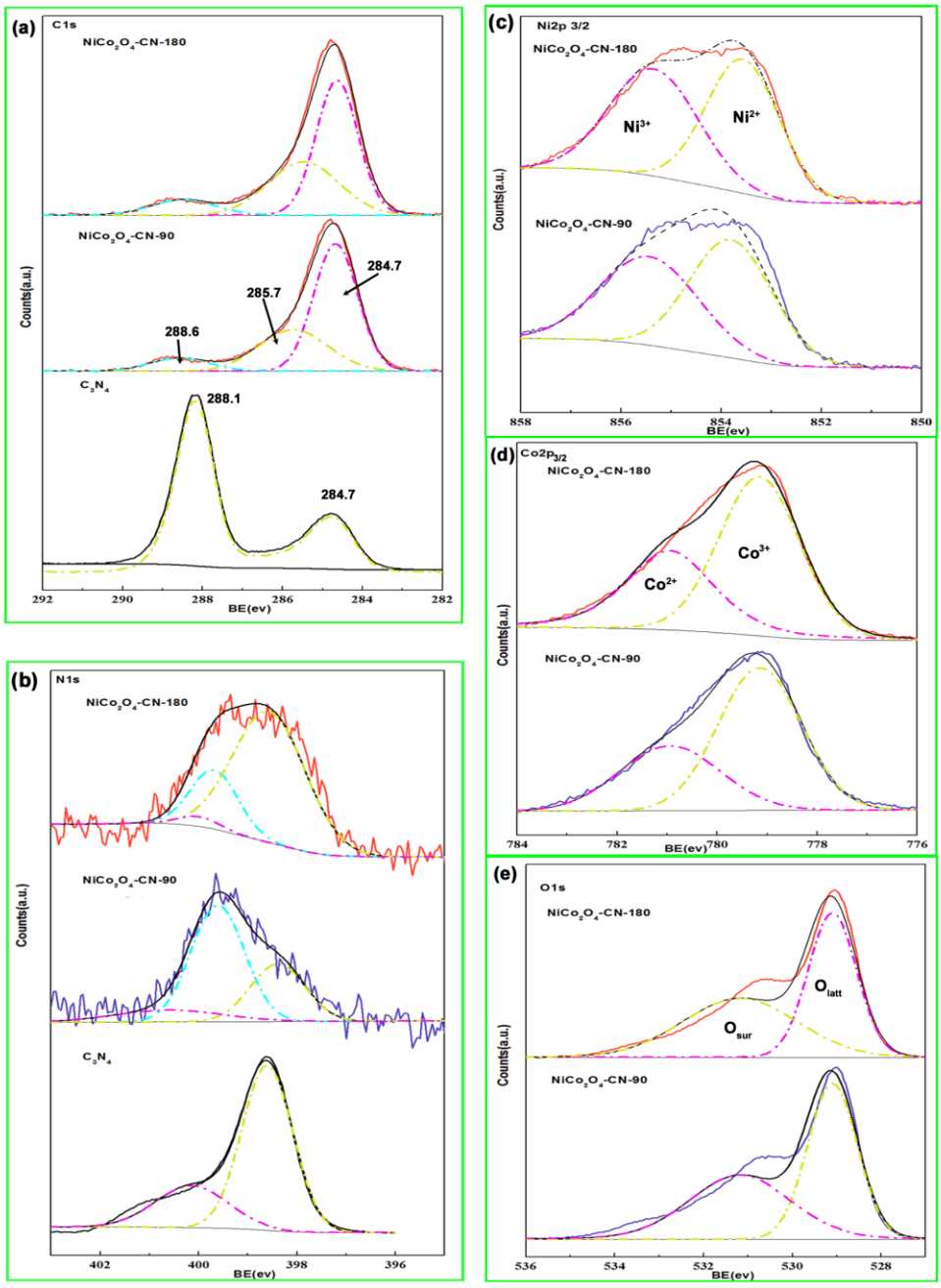

Fig.4 XPS spectra (a, C1s; b, N1s; c, Ni2p; d, Co2p; e, O1s)

To investigate the surface composition and the valence states of the samples, XPS characterization was performed. The full-scan XPS spectra was shown in Fig.S6 (Supporting information), which display the peaks corresponding to C1s, N1s, Ni2p, Co2p and O1s[8]. The C1s spectra of the $NiCo_2O_4$ and pure *g*-C_3N_4 are shown in Fig.4a. As for *g*-C_3N_4, two distinct peaks locate at about 288.1 and 284.7 eV can be observed,

and the first peak is related to the sp^2-hybridized carbon in the N-C=N aromatic ring of the *g*-C_3N_4 structure, the second peak can be attributed to sp^2 C-C bonds [29, 30]. In contrast, great changes happen over the C1s peaks of the two $NiCo_2O_4$-CN samples. The characteristic peak at 288.1 eV identified as *g*-C_3N_4 structure disappears and a series of continuous peaks appear, which could be fitted into three subpeaks at 284.7 (C=C), 285.7 eV (C-N) and 288.6 eV (O=C-O)[31]. This phenomenon indicates that *g*-C_3N_4 converts into N doped carbon under the reaction conditions, this is why the XRD test shows no sign of *g*-C_3N_4 pattern. Such a conversion could be further proved by the N1s result (Fig.4b). The N1s spectrum of *g*-C_3N_4 can be deconvoluted into two peaks: The major peak with binding energy (BE) of 398.6 represents the characteristic structure of sp^2-hybridized nitrogen in C-N=C ring, and the other minor peak at 400.1 eV stands for the N(-C_3) structure from *g*-C_3N_4[29]. As expected, the N1s spectra of the $NiCo_2O_4$-CN samples show different peaks to that of C_3N_4. The N1s can be fitted into three bands assigning to pyridinic-N (398.5 eV), pyrrolic-N (399.6 eV), and graphitic-N(400.1 eV), which suggest that the conversion of *g*-C_3N_4 to N-doped carbon[25, 31]. Based on the C1s and N1s results, *g*-C_3N_4 was successfully converted into N-doped carbon (CN), and this agrees well with the EDX and FT-IR results.

When considering Ni 2p spectra in Fig. S7 (Supporting information), two main peaks at about 855.0 eV for $Ni2p_{3/2}$ and 872.0 eV for $Ni2p_{1/2}$ with two satellites at 860.8 and 879.4 eV are observed. The Co 2p spectra show two sharp peaks centered at 779.0 eV for $Co2p_{3/2}$ and 794.3 eV for $Co2p_{1/2}$ together with two weak shake-up satellites. The Ni $2p_{3/2}$ and $Co2p_{3/2}$ were further fitted into two subpeaks in Fig. 4(c-d). From Fig.4c, the Ni $2p_{3/2}$ signals at 853.6 eV and 855.3 eV could be assigned to Ni^{2+} and Ni^{3+}, respectively. From Fig.4d, we can detect two subpeaks locating at 780.9 eV and 779.1 eV, demonstrating the co-existence of Co^{2+} and Co^{3+}, respectively. According to the peak fitting result, the molar ratio of Ni^{2+} to Ni^{3+} and Co^{2+} to Co^{3+} was calculated. The atomic ratio of Ni^{2+}/Ni^{3+} and Co^{2+}/Co^{3+} for $NiCo_2O_4$-CN-90 is 1.12 and 0.55, respectively. For $NiCo_2O_4$-CN-180, the value changes to 1.00 and 0.64,respectively. The O1s spectra in Fig.4e can be deconvoluted into two peaks: 529.1 and 531.9 eV,

which correspond to the lattice oxygen (O_{latt}) and the surface oxygen or defect oxygen(O_{sur}),respectively [11, 13, 32]. The atomic ratio of O_{sur}/O_{latt} is calculated based on the peak fitting result, and it shows an order of $NiCo_2O_4$-CN-180 (0.97) > $NiCo_2O_4$-CN-90 (0.88).

3.2 Electrocatalytic activities

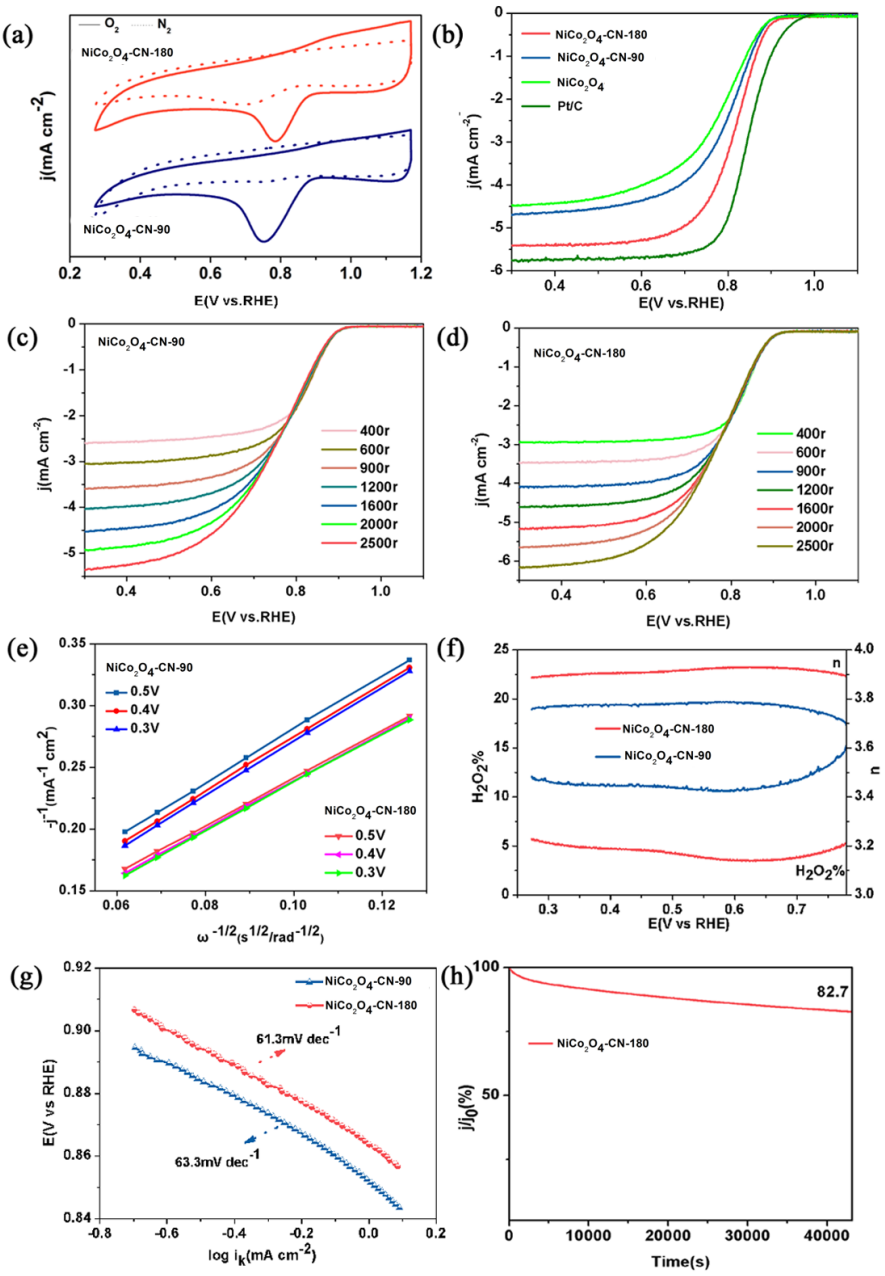

Fig.5 ORR performance (a) Cyclic voltammograms in N_2- and O_2-saturated 0.1 M KOH, (b) linear sweep voltammetries at a rotation speed of 1600 rpm, (c-d) LSVs of $NiCo_2O_4$

catalysts under different rotating rates of the disk electrode, (e) Koutecky-Levich (K-L) plots at different potentials, (f) plots of the hydrogen peroxide yields and electron-transfer numbers, (g) corresponding Tafel plots. (h) Chronoamperometric responses of the $NiCo_2O_4$-CN-180 catalysts over 12 h.

The ORR activity was first investigated by Cyclic voltammograms (CV) in 0.1 M KOH electrolyte (Fig.5a). When tested in O_2-saturated KOH electrolyte, we can observe obvious oxygen reduction characteristic peaks from both $NiCo_2O_4$ catalysts. Especially, $NiCo_2O_4$-CN-180 displays a more positive reduction peak compare to the $NiCo_2O_4$-CN-90, indicating its superior ORR activity. No distinct peak is found in N_2-saturated KOH electrolyte.

Linear scan voltammeter (LSV) curves tested by rotating disk electrode (RDE) at 1600 rpm (Fig.5b). Half-wave potential ($E_{1/2}$, the potential at a current density of 3 mA cm^{-2}) and diffusion-limiting current density was used for comparing the activity. The commercial Pt/C shows the best ORR activity. $NiCo_2O_4$-CN-180 exhibits a more positive $E_{1/2}$ of 0.81 V and a larger limiting current density of 5.4 mA cm^{-2}, which outperforms its counterpart $NiCo_2O_4$-CN-90 (0.77 V and 4.7 mA cm^{-2}). Without C_3N_4 used in the preparation process, the obtained pure $NiCo_2O_4$ shows a lower ORR performance with $E_{1/2}$ of 0.74 V and a larger limiting current density of 4.5 mA cm^{-2}. The ORR activity of $NiCo_2O_4$-CN-180 is compared with some recent published $NiCo_2O_4$ related papers (Table S1, Supporting information), clearly, $NiCo_2O_4$-CN-180 exhibits outstanding ORR performance among these results.

ORR polarization curves at different rotation rates are recorded and plotted in Fig.5(c-d) to extract the pertinent kinetic parameters. The curves have similar trends, and the reduction currents gradually increase with increasing rotation rate, which is related to the faster oxygen transfer near the electrode surface[33]. Based on Fig.5(c-d), the corresponding K–L plots were obtained in Fig.5e. From, Fig.5e, all the plots shows linearity, indicating first-order reaction kinetics towards oxygen over the

catalysts[12]. Furthermore, the plots of $NiCo_2O_4$-CN-180 has a relatively smaller intercept than its counterpart, manifesting that the number of electrons transferred during the ORR process over $NiCo_2O_4$-CN-180 is even larger, and more close to the four-electron process. The ORR process may follow two-electron or four-electron transfer mechanism, of which the later is more favorable and even high-efficiency. The ORR over $NiCo_2O_4$ based material normally follows the four-electron process[19, 21, 34]. As for ORR, there are two methods to calculate the electron transfer number (*n*), one is by the K-L plots in Fig.5e, especially involving with the intercept(the smaller intercept, the bigger *n*)[19], but the result of this method is relatively rough; And the more accurate method is through rotating-ring disk electrode. To obtain the accurate electron transfer number(*n*) and the yield of hydrogen peroxide ($y_{peroxide}$), they were further calculated by rotating-ring disk electrode (RRDE) as shown in Fig.5f. The *n* for $NiCo_2O_4$-CN-180 is around 3.90 and 3.72-3.77 for $NiCo_2O_4$-CN-90 over the potential range of 0.3-0.75 V, and this indicates that both catalysts follow an apparent 4 electron reduction pathway. Considering the $y_{peroxide}$, $NiCo_2O_4$-CN-90 displays a much higher yield of above 11.6% than that of the $NiCo_2O_4$-CN(below 5.3%). The relatively larger *n* and smaller $y_{peroxide}$ prove the superior ORR activities of $NiCo_2O_4$-CN-180. The Tafel plots are shown in Fig.5g. Comparing to $NiCo_2O_4$-CN-90, $NiCo_2O_4$-CN-180 has a smaller slope of 61.3 mV dec^{-1}), manifesting the fastest ORR kinetics. $NiCo_2O_4$-CN-180 also exhibits outstanding long-term durability for ORR. Fig. 5h shows the chronoamperometric responses at the potential of 0.50 V. The chronoamperometric measurement for 12 h confirms that $NiCo_2O_4$-CN-180 has s a higher retention rate of 82.7%.

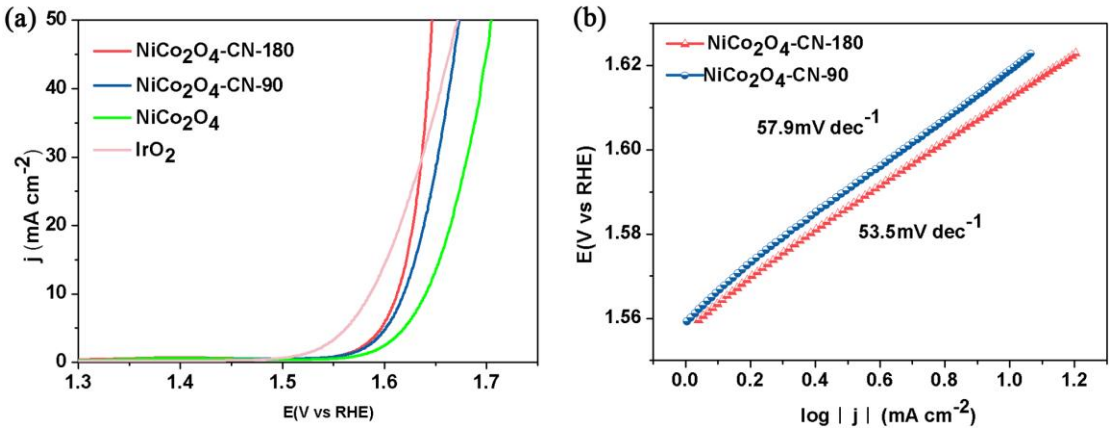

Fig.6 OER performance. (a) LSV curves at a rotation speed of 1600 rpm, (b) Tafel plots of $NiCo_2O_4$ catalysts.

The OER performance of the catalysts was tested by LSVs on rotating disk electrode in 1.0 M KOH electrolyte (Fig.6a). For OER, the overpotential (η_{10}) to reach a current density of 10 mA cm^{-2} is often used as a scale to evaluate the OER performance[35]. To reach a current density of 10 mA cm^{-2}, the overpotential (η_{10}) for $NiCo_2O_4$-CN-180 is 383 mV, which is better than that of $NiCo_2O_4$-CN-90 (389 mV) and pure $NiCo_2O_4$ (411 mV), but inferior to that of the commercial IrO_2 (356 mV). Tafel slope is commonly applied to understand the reaction kinetics, and the slope is a kinetic descriptor that provides information on the electrochemical mechanism[35, 36]. Therefore, Tafel plots of the polarization curves were calculated to further prove the superior performance of $NiCo_2O_4$-CN-180. As shown in Fig.6b, the Tafel slope of $NiCo_2O_4$-CN-180 is 53.5 mV dec^{-1}, while $NiCo_2O_4$-CN-90 displays a larger Tafel slope of 57.9 mV dec^{-1}. This result indicates that $NiCo_2O_4$-CN-180 exhibits a higher OER rate and favorable kinetics.

The potential gap, ΔE, between the potential at 10 mA cm^{-2} of OER and half-wave potential of ORR could be used as a benchmark to judge the overall bifunctional ORR/OER activities[12, 15], the smaller the ΔE, the better the electrochemical performance. The ΔE of the samples was calculated and showed in Fig.S8 (Supporting information). Obviously, the ΔE rises in the order of $NiCo_2O_4$-CN-180

(0.80 V)< $NiCo_2O_4$-CN-90 (0.85 V)< $NiCo_2O_4$ (0.90 V), indicating that the overall bifunctional ORR/OER performance rises in the opposite order.

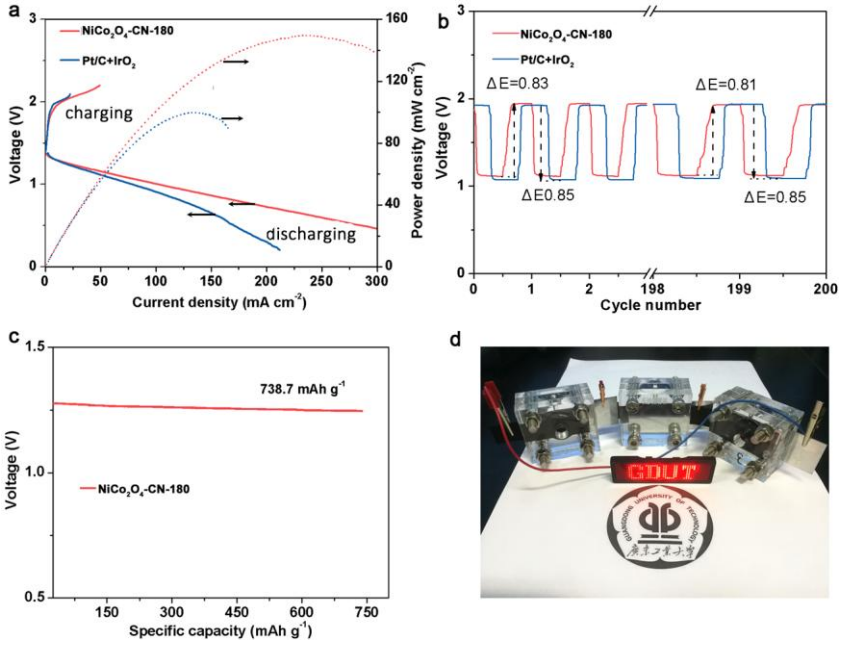

Fig.7 the performance of Zn-air battery using $NiCo_2O_4$-C/N-180 and noble metal as electrode catalysts (a)charging and discharging polarization and power density curves , (b) cycling performance, (c) discharge curves at 5.0 mA cm^{-2}, (d) LED powered by the $NiCo_2O_4$-CN battery

As $NiCo_2O_4$-CN-180 displays superior bifunctional ORR/OER activities, we further assembled a home-made Zn-air battery using it as cathode catalyst and zinc plate as the anode. We also fabricated a zinc-air battery using commercial 20%Pt/C and IrO_2. The corresponding performance is shown in Fig.7. From Fig.7a, the Zn-air battery based on $NiCo_2O_4$-CN-180 has a relatively high peak power density, reaching 149.6 mW cm^{-2} at a current density of 235.7mA cm^{-2}, which is much better than that of assembled by 20%Pt/C and IrO_2 (99.6mW cm^{-2} at 131.5 mA cm^{-2}). Stability is a key parameter of the Zn-air battery, therefore, cycle stability was measured at a current density of 5mA cm^{-2} for 200 cycles (Fig.7b). The $NiCo_2O_4$-CN-180 shows a higher discharge platform, about 40 mV, than the noble metal. As for the charging platform, at the initial stage, the noble metal is slightly better than the $NiCo_2O_4$-CN-180.

Whereas, after 100 cycles, the charging platform of $NiCo_2O_4$-CN-180 is slowly leveled with the noble metal and then surpasses. The $NiCo_2O_4$-CN-180 exhibits excellent cycling stability, after 200 cycles of testing, the performance is almost unchanged. The capacity test result is shown in Fig.7c. The $NiCo_2O_4$-CN-180 battery possesses excellent capacity performance up to 738.7 mAh g^{-1}. The $NiCo_2O_4$-CN battery can effectively illuminate a 3V LED as displayed in Fig.7d, which indicates its practical application.

3.3 Discussion

The electrochemical reaction of ORR/OER is a very complex process involving a three-phase interface (gas-liquid-solid)[37]. The activity difference can not be solely attributed to a particular parameter. It is the synergistic effects of catalyst that lead to a superior overall electrochemical performance.

BET and pore size distribution. From the point of macro-structure engineering of superior ORR/OER catalysts**,** the porous structure with larger BET area and rich mesopores/macropores are highly required. A porous structure benefits the diffusion of oxygen over the catalyst and facilitate fast ion and electron transfer by providing effective pathways and channels [37]. From Fig.3, the BET surface area of $NiCo_2O_4$-CN-180 (84.22 m^2 g^{-1}) is slightly larger than that of $NiCo_2O_4$-CN-90 (78.10 m^2 g^{-1}), however, its pore size distribution is relatively smaller than that of its counterpart. This result suggests that $NiCo_2O_4$-180 could provide more active sites and increased contact area for ORR/OER, but its transfer ability might be inferior to $NiCo_2O_4$-CN-90.

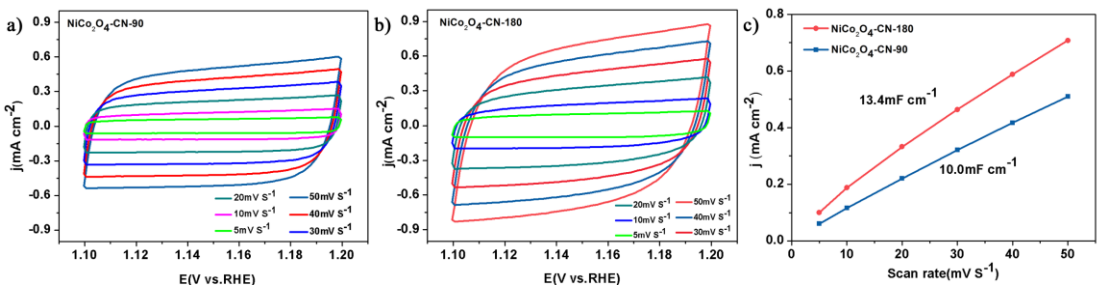

Fig.8 ECSA evaluation for CV activation. (a-b) Typical cyclic voltammetry curves at different scan rates, (c) Charging current density differences plotted against scan rates.

ECSA. To explain the performance difference, the ECSA is often used to illustrate the active surface area of the catalysts, which can reflect the true contact area involved in the electrochemical reaction. The electrochemical double-layer capacitance (C_{dl}) is linearly proportional to ECSA, and is widely used to represent ECSA[38, 39]. Therefore，the C_{dl} is computed by CV curves under different scan rates and shown in Fig.8(a-b). From the slope of the linear relationship in Fig.8c, the C_{dl} could be calculated. Apparently, $NiCo_2O_4$-CN-180 exhibits higher C_{dl} (13.4 mF cm^{-1}) than that of $NiCo_2O_4$-CN-90 (10.0 mF cm^{-1}), suggesting that the former has bigger ECSA and more accessible active sites for the electrochemical reactions[38]. The larger ECSA contributes to superior ORR/OER performance.

Oxygen species. The ORR/OER is the process involving oxygen oxidation and reduction, and oxygen species especially oxygen defects/vacancies of metal oxides have a vital influence on the activities[40-44]. The role of oxygen vacancies for metal oxides includes: being active sites for ORR/OER and being shallow donors to enhance electrical conductivity[40]. Bearing this in mind, the engineering of oxygen defect has been proved to be an effective strategy to enhance the electrochemical activity. From the O 1s peak fitting result in Fig.4e, $NiCo_2O_4$-CN-180 possesses a relatively larger amount of defect oxygen than that of $NiCo_2O_4$-CN-90, and this favor for its outstanding electrochemical activity.

Metal valence: Metal valence in spinel structure has a great effect on the ORR/OER activities[45]. The metal valence could affect the electronic structure induced by the Jahn-Teller effect and affect the interaction with oxygen[46]. For example, the valence of Mn displayed a volcano trend for the $MnCo_2O_4$ in ORR process, of which the $Mn^{3.4+}$ showed the best ORR performance; while for OER process, the superior activity was obtained on the relatively lower valence of Mn [46]. Therefore, it is

important to gain a balance/compromise of metal valence in spinel oxide when using for bifunctional ORR/OER catalyst. As for spinels with AB_2O_4 structure, the metal A usually occupies tetrahedral sites with +2 valence, and metal B holds octahedral sites with +3 or +2 valence[47]. More specifically, considering $NiCo_2O_4$, Ni and Co have similar radii and valence(+2, +3), and different synthesis condition could lead to the coexistence of various valence (+2 and +3)of the same metal[48]. Therefore, Ni and Co could hold both the tetrahedral and octahedral sites, and this could lead to a different molar ratios of Ni^{2+}/Ni^{3+} and Co^{2+}/Co^{3+}. Deng's report showed that the nickel-cobalt oxide with higher Ni^{3+}/Ni^{2+} and lower Co^{3+}/Co^{2+} exhibited the best OER/ORR performance[34]. A similar conclusion was obtained by Huang, et al [45], the minor doping Fe to $NiCo_2O_4$ induce increased ratio of Ni^{3+}/Ni^{2+} and decreased Co^{3+}/Co^{2+}, which leads to enhanced OER performance. Yang et al[17] concluded that Ni^{3+} instead of Co was vital for OER, and higher Ni^{3+}/Ni^{2+} was preferred. As some other literature reported, Co^{2+} was regarded as the active sites for ORR and Ni^{3+} for OER[34, 49, 50]. In our case, as the XPS results showed, $NiCo_2O_4$-CN-180 displayed relatively more Ni^3 and Co^{2+} comparing to $NiCo_2O_4$-CN-90, and this characteristic leads to its excellent ORR/OER performance. Some facts about the enhancement mechanism include: More Ni^{3+} present in octahedral sites could greatly increase the conductivity of nickel cobalt oxide even to five orders of magnitude[51]. The better conductivity is what an outstanding electrochemical catalyst required; More Co^{2+} presents suggest more oxygen vacancies[41], which is beneficial for the ORR/OER process; the enriched Ni^{3+} and Co^{2+} species favors the activation of oxygen species, and accelerates the overall reaction kinetics[34].

Effect of N species. The doping of N can effectively enhance the ORR/OER performance of all kinds of carbon materials. Based on XPS analysis, normally, three kinds of N could be detected: pyridinic N, pyrrolic N and graphitic (or quaternary) N. Until now, great distributes still exist as to which kind of N is prevailing in ORR/OER process. However, two facts seem to be confirmed[52, 53]: (1) pyridinic N and graphitic N outperform pyrrolic N, and the former two are equally important, the

latter almost makes no contribution to the catalysis; (2)The total content of N has no visible correlation with ORR activity while there might be changes in the amount of different kind of N species. From the N1s peak fitting result, we could calculate the molar ratio of (pyridinic N+graphitic N)/(pyrrolic N). Obviously, the ratio rises from 1.17 for $NiCo_2O_4$-CN-90 to 3.53 for $NiCo_2O_4$-CN-180, and this fact confirms that $NiCo_2O_4$-CN-180 processes more active N species, which could contribute a lot to the enhancement of the ORR/OER performance.

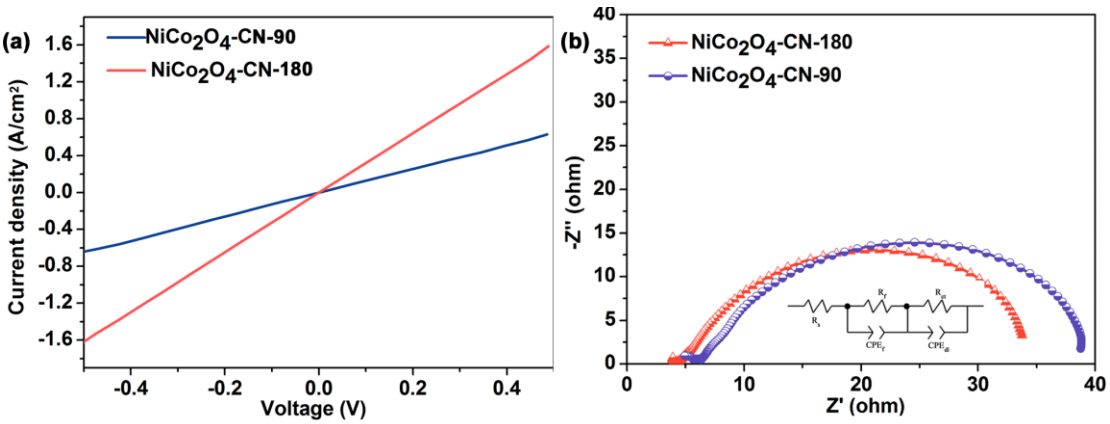

Fig. 9 (a) I-V curves of the $NiCo_2O_4$ catalysts; (b) Nyquist plots from EIS measurements.

Conductivity. The conductivity of the materials was tested by a two-point approach. The I-V curves for the two different catalysts are shown in Fig.9a. The slope of the I-V curve of $NiCo_2O_4$-CN-180 is larger than that of $NiCo_2O_4$-CN-90, indicating that the former has better conductivity and is more conducive for the rapid transfer of electrons. The better conductivity of $NiCo_2O_4$-CN-180 should be mainly due to the carbonization of *g*-C_3N_4 and also the appropriate Ni^{3+} as aforementioned discussion.

Reaction kinetics. The ionic and charge transportation play an important role in the ORR/OER process. Electrochemical impedance spectroscopy (EIS) was taken to study the kinetics process, and the corresponding Nyquist plots and fitted circuit are shown in Fig.9b. In the fitted circuit, the R_s is related with the uncompensated solution

resistance, R_f and CPE_f reflect the intrinsic resistance of the catalyst and constant phase element of the catalysts layer. While, R_{ct} and CPE_{dl} stands for the charge transfer resistance and the constant phase element of the double layer[54]. In high frequency regime, the $NiCo_2O_4$-CN-180 displays a smaller intercept in the real axis than that of $NiCo_2O_4$-CN-90, indicating its relatively lower contact resistance and ohmic resistance. Furthermore, $NiCo_2O_4$-CN-180 exhibits the smaller semicircle comparing to that of $NiCo_2O_4$-CN-90, and the fitted charge-transfer resistance (R_{ct}) is 31.8 Ω and 34.4Ω for $NiCo_2O_4$-CN-180 and $NiCo_2O_4$-CN-90, respectively. The smaller Rct of $NiCo_2O_4$-CN-180 indicates its faster and better kinetics process.

4. Conclusions

In summary, we have constructed a 3D composite $NiCo_2O_4$-CN catalyst composing of interconneted $NiCo_2O_4$ nanosheets and N-doped carbon with different content of N via adjusting the solvothermal temperature. The $NiCo_2O_4$-CN-180 catalyst exhibits enhanced ORR activity with a half-wave potential of 0.81 V, a limiting current density of 5.4 mA cm^{-2}, an electronic transfer number of 3.90, and a Tafel slope of 61.3 mV dec^{-1}, and improved OER performance with smaller overpotential (383 mV) and Tafel slope (53.5 mV dec^{-1}). When assembling into a portable Zn-air battery, the $NiCo_2O_4$-CN-180 exhibits comparable performance to the commercial Pt/C and IrO_2. Such impressive bi-functional ORR/OER performance of the composite electrocatalyst is mainly attributed to the collective effects of porous 3D structure, larger ECSA, richer defect oxygen, relatively higher Ni^3 and Co^{2+}, more active pyridinic N+graphitic N species, better conductivity, and enhanced charge-transfer ability. Our findings demonstrate that the combination of $NiCo_2O_4$ with N-doped carbon is an effective way to construct bi-functional ORR/OER electrocatalyst with improved activities. Therefore, future work could be performed on searching for more interesting N-doped carbon material as carrier/composition for $NiCo_2O_4$ based ORR/OER catalytast. The carbon material could be from metal-organic frameworks, or prussian blue analogs, or other biomass based carbon.Furthermore, the integrated

$NiCo_2O_4$ catalyst could also be assembled into portable solid-state Zn-air battery for the application of wearable electronic devices.

Acknowledgements

This work was supported by the National Natural Science Foundation of China (21576054); Science and Technology Planning Project of Guangdong Province (2016A010104017); and the Foundation of Higher Education of Guangdong Province (2015KTSCX027, 2018KZDXM031).

Reference

[1] Z.-F. Huang, J. Wang, Y. Peng, C.-Y. Jung, A. Fisher, X. Wang, Design of Efficient Bifunctional Oxygen Reduction/Evolution Electrocatalyst: Recent Advances and Perspectives, Adv.Energy Mater., 7 (2017) 1700544.

[2] D.U. Lee, P. Xu, Z.P. Cano, A.G. Kashkooli, M.G. Park, Z.W. Chen, Recent progress and perspectives on bi-functional oxygen electrocatalysts for advanced rechargeable metal-air batteries, J. Mater. Chem. A, 4 (2016) 7107-7134.

[3] G. Fu, X. Yan, Y. Chen, L. Xu, D. Sun, J.-M. Lee, Y. Tang, Boosting Bifunctional Oxygen Electrocatalysis with 3D Graphene Aerogel-Supported Ni/MnO Particles, Adv. Mater., 30 (2018) 1704609.

[4] C. Si, Y. Zhang, C. Zhang, H. Gao, W. Ma, L. Lv, Z. Zhang, Mesoporous nanostructured spinel-type MFe_2O_4 (M=Co, Mn, Ni) oxides as efficient bi-functional electrocatalysts towards oxygen reduction and oxygen evolution, Electrochim. Acta, 245 (2017) 829-838.

[5] D. Yang, L. Zhang, X. Yan, X. Yao, Recent Progress in Oxygen Electrocatalysts for Zinc-Air Batteries, Small Methods, 1 (2017) 1700209.

[6] W. Shang, W. Yu, P. Tan, B. Chen, H. Xu, M. Ni, A high-performance Zn battery based on self-assembled nanostructured $NiCo_2O_4$ electrode, J Power Soucrces, 421 (2019) 6-13.

[7] C. Jin, F. Lu, X. Cao, Z. Yang, R. Yang, Facile synthesis and excellent electrochemical properties of $NiCo_2O_4$ spinel nanowire arrays as a bifunctional catalyst for the oxygen reduction and evolution reaction, J. Mater. Chem. A, 1 (2013) 12170.

[8] D.U. Lee, B.J. Kim, Z. Chen, One-pot synthesis of a mesoporous $NiCo_2O_4$ nanoplatelet and graphene hybrid and its oxygen reduction and evolution activities as an efficient bi-functional electrocatalyst, J. Mater. Chem. A, 1 (2013) 4754.

[9] J. Wang, Y. Fu, Y.J. Xu, J. Wu, J.H. Tian, R.Z. Yang, Hierarchical $NiCo_2O_4$ hollow nanospheres as high efficient bi-functional catalysts for oxygen reduction and evolution reactions, Int. J. Hydrogen Energy, 41 (2016) 8847-8854.

[10] H. Fu, Y. Liu, L. Chen, Y. Shi, W. Kong, J. Hou, F. Yu, T. Wei, H. Wang, X. Guo, Designed formation of $NiCo_2O_4$ with different morphologies self-assembled from nanoparticles for asymmetric supercapacitors and electrocatalysts for oxygen evolution reaction, Electrochim. Acta, 296 (2019)

719-729.
[11] W. Liu, J. Bao, L. Xu, M. Guan, Z. Wang, J. Qiu, Y. Huang, J. Xia, Y. Lei, H. Li, $NiCo_2O_4$ ultrathin nanosheets with oxygen vacancies as bifunctional electrocatalysts for Zn-air battery, Appl. Sur. Sci., 478 (2019) 552-559.
[12] Y. Huang, F. Cui, Y. Zhao, J. Bao, J. Lian, Y. Xu, T. Liu, H. Li, Controllable Synthesis of Ultrathin $NiCo_2O_4$ Nanosheets Incorporated onto Composite Nanotubes for Efficient Oxygen Reduction, Chem., Asian J., 12 (2017) 2426-2433.
[13] M. Yang, Y. Li, Y. Yu, X. Liu, Z. Shi, Y. Xing, Self-Assembly of Three-Dimensional Zinc-Doped $NiCo_2O_4$ as Efficient Electrocatalysts for Oxygen Evolution Reaction, Chem., 24 (2018) 13002-13008.
[14] Y.-T. Lu, Y.-J. Chien, C.-F. Liu, T.-H. You, C.-C. Hu, Active site-engineered bifunctional electrocatalysts of ternary spinel oxides, $M_{0.1}Ni_{0.9}Co_2O_4$ (M: Mn, Fe, Cu, Zn) for the air electrode of rechargeable zinc–air batteries, J. Mater. Chem. A, 5 (2017) 21016-21026.
[15] C. Han, W. Li, H.-K. Liu, S. Dou, J. Wang, Design strategies for developing non-precious metal based bi-functional catalysts for alkaline electrolyte based zinc–air batteries, Mater. Horiz., (2019).
[16] Y. Wang, J. Li, Z. Wei, Transition-metal-oxide-based catalysts for the oxygen reduction reaction, J. Mater. Chem. A, 6 (2018) 8194-8209.
[17] Y. Liu, P. Liu, W. Qin, X. Wu, G. Yang, Laser modification-induced $NiCo_2O_{4-\delta}$ with high exterior Ni^{3+}/Ni^{2+} ratio and substantial oxygen vacancies for electrocatalysis, Electrochim. Acta, 297 (2019) 623-632.
[18] Y.-J. Wang, H. Fan, A. Ignaszak, L. Zhang, S. Shao, D.P. Wilkinson, J. Zhang, Compositing doped-carbon with metals, non-metals, metal oxides, metal nitrides and other materials to form bifunctional electrocatalysts to enhance metal-air battery oxygen reduction and evolution reactions, Chem. Eng. J., 348 (2018) 416-437.
[19] S. Jiang, K. Ithisuphalap, X. Zeng, G. Wu, H. Yang, 3D porous cellular $NiCoO_2$/graphene network as a durable bifunctional electrocatalyst for oxygen evolution and reduction reactions, J. Power Soucrces, 399 (2018) 66-75.
[20] H. Zhang, H. Qiao, H. Wang, N. Zhou, J. Chen, Y. Tang, J. Li, C. Huang, Nickel cobalt oxide/carbon nanotubes hybrid as a high-performance electrocatalyst for metal/air battery, Nanoscale, 6 (2014) 10235-10242.
[21] J. Wang, Z. Wu, L. Han, R. Lin, H.L. Xin, D. Wang, Hollow-Structured Carbon-Supported Nickel Cobaltite Nanoparticles as an Efficient Bifunctional Electrocatalyst for the Oxygen Reduction and Evolution Reactions, ChemCatChem, 8 (2016) 736-742.
[22] H. Ge, G. Li, T. Zheng, F. Wang, M. Shao, H. Liu, X. Meng, Hollow $NiCo_2O_4$ nanospheres supported on N-doped carbon nanowebs as efficient bifunctional catalyst for rechargeable and flexible Zn-air batteries, Electrochim. Acta, 319 (2019) 1-9.
[23] J. Bao, X. Zhang, B. Fan, J. Zhang, M. Zhou, W. Yang, X. Hu, H. Wang, B. Pan, Y. Xie, Ultrathin Spinel-Structured Nanosheets Rich in Oxygen Deficiencies for Enhanced Electrocatalytic Water Oxidation, Angew. Chem.Int .Ed., 54 (2015) 7399-7404.
[24] H. Yu, L. Shang, T. Bian, R. Shi, G.I. Waterhouse, Y. Zhao, C. Zhou, L.Z. Wu, C.H. Tung, T. Zhang, Nitrogen-Doped Porous Carbon Nanosheets Templated from g-C_3N_4 as Metal-Free Electrocatalysts for Efficient Oxygen Reduction Reaction, Adv. Mater., 28 (2016) 5080-5086.
[25] Q. Li, D. Xu, X. Ou, F. Yan, Nitrogen-Doped Graphitic Porous Carbon Nanosheets Derived from In Situ Formed g-C_3N_4 Templates for the Oxygen Reduction Reaction, Chem. Asian J., 12 (2017) 1816-1823.

[26] Z. Xu, J. Ma, M. Shi, Y. Xie, C. Feng, Biomass based iron and nitrogen co-doped 3D porous carbon as an efficient oxygen reduction catalyst, J. Colloid. Interface Sci., 523 (2018) 144-150.

[27] S.-H. Bae, J.-E. Kim, H. Randriamahazaka, S.-Y. Moon, J.-Y. Park, I.-K. Oh, Seamlessly Conductive 3D Nanoarchitecture of Core-Shell Ni-Co Nanowire Network for Highly Efficient Oxygen Evolution, Adv.Energy Mater., 7 (2017) 1601492.

[28] H. Gao, R. Cao, S. Zhang, H. Yang, X. Xu, Three-Dimensional Hierarchical g-C_3N_4 Architectures Assembled by Ultrathin Self-Doped Nanosheets: Extremely Facile Hexamethylenetetramine Activation and Superior Photocatalytic Hydrogen Evolution, ACS Appl.Mater. Inerfaces, 11 (2019) 2050-2059.

[29] Y. Qiu, L. Xin, F. Jia, J. Xie, W. Li, Three-Dimensional Phosphorus-Doped Graphitic-C_3N_4 Self-Assembly with NH_2-Functionalized Carbon Composite Materials for Enhanced Oxygen Reduction Reaction, Langmuir, 32 (2016) 12569-12578.

[30] S. Yang, Y. Gong, J. Zhang, L. Zhan, L. Ma, Z. Fang, R. Vajtai, X. Wang, P.M. Ajayan, Exfoliated graphitic carbon nitride nanosheets as efficient catalysts for hydrogen evolution under visible light, Adv. Mater. 25 (2013) 2452-2456.

[31] R. Boppella, J. Tan, W. Yang, J. Moon, Homologous CoP/NiCoP Heterostructure on N-Doped Carbon for Highly Efficient and pH-Universal Hydrogen Evolution Electrocatalysis, Adv. Funct. Mater., 29 (2018) 1807976.

[32] S. Lin, X. Shi, H. Yang, D. Fan, Y. Wang, K. Bi, Reduced graphene oxide-$NiCo_2O_4$ nanoflowers as efficient electrocatalysts for the oxygen reduction reaction, J. Alloys Comp., 720 (2017) 147-155.

[33] Y. He, J. Zhang, G. He, X. Han, X. Zheng, C. Zhong, W. Hu, Y. Deng, Ultrathin Co_3O_4 nanofilm as an efficient bifunctional catalyst for oxygen evolution and reduction reaction in rechargeable zinc-air batteries, Nanoscale, 9 (2017) 8623-8630.

[34] J. Zhao, Y. He, Z. Chen, X. Zheng, X. Han, D. Rao, C. Zhong, W. Hu, Y. Deng, Engineering the Surface Metal Active Sites of Nickel Cobalt Oxide Nanoplates toward Enhanced Oxygen Electrocatalysis for Zn-Air Battery, ACS Appl. Mater. Interfaces, 11 (2019) 4915-4921.

[35] M. Tahir, L. Pan, F. Idrees, X. Zhang, L. Wang, J.-J. Zou, Z.L. Wang, Electrocatalytic oxygen evolution reaction for energy conversion and storage: A comprehensive review, Nano Energy, 37 (2017) 136-157.

[36] M.B. Stevens, L.J. Enman, A.S. Batchellor, M.R. Cosby, A.E. Vise, C.D.M. Trang, S.W. Boettcher, Measurement Techniques for the Study of Thin Film Heterogeneous Water Oxidation Electrocatalysts, Chem. Mater., 29 (2016) 120-140.

[37] X. Cai, L. Lai, J. Lin, Z. Shen, Recent advances in air electrodes for Zn–air batteries: electrocatalysis and structural design, Mater. Horiz.,, 4 (2017) 945-976.

[38] H. Jiang, Q. He, X. Li, X. Su, Y. Zhang, S. Chen, S. Zhang, G. Zhang, J. Jiang, Y. Luo, P.M. Ajayan, L. Song, Tracking Structural Self-Reconstruction and Identifying True Active Sites toward Cobalt Oxychloride Precatalyst of Oxygen Evolution Reaction, Adv. Mater., 31 (2019) e1805127.

[39] J. Joo, T. Kim, J. Lee, S.I. Choi, K. Lee, Morphology-Controlled Metal Sulfides and Phosphides for Electrochemical Water Splitting, Adv. Mater., 31 (2019) e1806682.

[40] D. Ji, L. Fan, L. Tao, Y. Sun, M. Li, G. Yang, T.Q. Tran, S. Ramakrishna, S. Guo, The Kirkendall Effect for Engineering Oxygen Vacancy of Hollow Co_3O_4 Nanoparticles toward High-Performance Portable Zinc-Air Batteries, Angew. Chem. Int. Ed., 58 (2019) 13840-13844.

[41] H. Yuan, J. Li, W. Yang, Z. Zhuang, Y. Zhao, L. He, L. Xu, X. Liao, R. Zhu, L. Mai, Oxygen Vacancy-Determined Highly Efficient Oxygen Reduction in $NiCo_2O_4$/Hollow Carbon Spheres, ACS

Appl. Mater. Interfaces, 10 (2018) 16410-16417.

[42] K. Zhang, G. Zhang, J. Qu, H. Liu, Disordering the Atomic Structure of Co(II) Oxide via B-Doping: An Efficient Oxygen Vacancy Introduction Approach for High Oxygen Evolution Reaction Electrocatalysts, Small, 14 (2018) 1802760.

[43] T. Ling, D.Y. Yan, Y. Jiao, H. Wang, Y. Zheng, X. Zheng, J. Mao, X.W. Du, Z. Hu, M. Jaroniec, S.Z. Qiao, Engineering surface atomic structure of single-crystal cobalt (II) oxide nanorods for superior electrocatalysis, Nat. Commun., 7 (2016) 12876.

[44] R. Gao, Z. Shang, L. Zheng, J. Wang, L. Sun, Z. Hu, X. Liu, Enhancing the Catalytic Activity of Co_3O_4 Nanosheets for Li-O_2 Batteries by the Incoporation of Oxygen Vacancy with Hydrazine Hydrate Reduction, Inorg. Chem., 58 (2019) 4989-4996.

[45] Y. Liu, Y. Ying, L. Fei, Q. Hu, G. Zhang, S.Y. Pang, W. Lu, C.L. Mak, X. Luo, L. Zhou, M. Wei, H. Huang, Valence Engineering via Selective Atomic Substitution on Tetrahedral Sites in Spinel Oxide for Highly Enhanced Oxygen Evolution Catalysis, J. Am. Chem. Soc., 141 (2019) 8136-8145.

[46] C. Wei, Z. Feng, G.G. Scherer, J. Barber, Y. Shao-Horn, Z.J. Xu, Cations in Octahedral Sites: A Descriptor for Oxygen Electrocatalysis on Transition-Metal Spinels, Adv. Mater., 29 (2017) 1606800-n/a.

[47] Q. Zhao, Z. Yan, C. Chen, J. Chen, Spinels: Controlled Preparation, Oxygen Reduction/Evolution Reaction Application, and Beyond, Chem. Rev., 117 (2017) 10121-10211.

[48] J.F. Marco, J.R. Gancedo, M. Gracia, J.L. Gautier, E. Ríos, F.J. Berry, Characterization of the Nickel Cobaltite, $NiCo_2O_4$, Prepared by Several Methods: An XRD, XANES, EXAFS, and XPS Study, J. Solid State Chem., 153 (2000) 74-81.

[49] J. Xiao, Q. Kuang, S. Yang, F. Xiao, S. Wang, L. Guo, Surface Structure Dependent Electrocatalytic Activity of Co_3O_4 Anchored on Graphene Sheets toward Oxygen Reduction Reaction, Sci.Rep., 3 (2013) 2300.

[50] J. Wang, R. Gao, D. Zhou, Z. Chen, Z. Wu, G. Schumacher, Z. Hu, X. Liu, Boosting the Electrocatalytic Activity of Co_3O_4 Nanosheets for a Li-O_2 Battery through Modulating Inner Oxygen Vacancy and Exterior Co^{3+}/Co^{2+} Ratio, ACS Catal., 7 (2017) 6533-6541.

[51] Y. Li, P. Hasin, Y. Wu, $Ni_xCo_{3-x}O_4$ nanowire arrays for electrocatalytic oxygen evolution, Adv. Mater., 22 (2010) 1926-1929.

[52] Z. Xia, L. An, P. Chen, D. Xia, Non-Pt Nanostructured Catalysts for Oxygen Reduction Reaction: Synthesis, Catalytic Activity and its Key Factors, Adv. Energy Mater., 6 (2016) 1600458.

[53] X. Huang, Y. Wang, W. Li, Y. Hou, Noble metal-free catalysts for oxygen reduction reaction, Sci. China Chem., 60 (2017) 1494-1507.

[54] X. Zhao, Y. Fu, J. Wang, Y. Xu, J.-H. Tian, R. Yang, Ni-doped $CoFe_2O_4$ Hollow Nanospheres as Efficient Bi-functional Catalysts, Electrochim. Acta, 201 (2016) 172-178.